The Astrophysical Journal, 889:28 (7pp), 2020 January 20 https://doi.org/10.3847/1538-4357/ab6334

Comparison of Kinematics of Solar Eruptive Prominences and Spatial Distribution of the Magnetic Decay Index

Ivan Myshyakov[1,3] and Tsvetan Tsvetkov[2]
[1] Institute of Solar-Terrestrial Physics, SB RAS, Russia; ivan_m@iszf.irk.ru
[2] Institute of Astronomy and National Astronomical Observatory, BAS, Bulgaria
Received 2019 July 1; revised 2019 December 17; accepted 2019 December 18; published 2020 January 22

Abstract

Theoretical studies of electric current instability explaining solar prominence eruptions show that the loss of equilibrium may develop in a case when the surrounding magnetic field decreases sufficiently rapidly with height. The magnetic decay index, a parameter indicating whether the external magnetic field has a configuration that may lead to a certain type of electric current instability, is a useful instrument for predicting the behavior of prominences. In our study, we consider three eruptive prominences. We perform potential-field extrapolation to obtain the spatial distribution of the magnetic decay index in the coronal space identified with the prominences. Analysis of time-dependent height profiles of the prominences revealed that eruptions started at heights close to those, where the computed magnetic decay index exceeded a value equal to 1.5. This indicates that the torus instability is a possible mechanism of the considered eruptive events.

Unified Astronomy Thesaurus concepts: Solar prominences (1519); Solar magnetic fields (1503); Eruptive phenomena (475)

1. Introduction

The difference between the physical properties of prominences and their surroundings shows that they are isolated formations separated from the corona by the prominence–corona transition region. They can be observed in emission on the solar limb (as prominences) or in absorption on the disk (as filaments). Both terms are related to the same structure, and the difference between them specifies only the place where the structure is noticed. Often prominences undergo destabilization and activation processes; from stable quiescent structures, they transform into active ones, changing their configuration, shape, and structure (Kilper et al. 2009). The development of different instabilities in parts of the Sun where a prominence forms is related to the enhancement of large-scale and/or inner motions of the material, which indicates an imminent prominence eruption. The dominance of the coronal magnetic field over gas pressure suggests that the plasma is "frozen" into the magnetic structure of eruptive prominences (EPs) and displays processes that reveal the structure and changes of the local coronal magnetic fields (Rompolt 1984).

Prominences are always situated above the magnetic inversion lines—the boundaries between regions with opposite magnetic polarity in the photosphere, where the magnetic field has only a horizontal component (Babcock & Babcock 1955). In the study by Kuperus & Raadu (1974), the authors showed that prominences formed in a magnetically neutral sheet resist the gravity supported by magnetic forces due to induced currents in the photospheric boundary. In this model, the straight horizontal electric current channel in the corona, together with its opposite mirror reflection below the photosphere, keeps the filament stable as a repulsive Lorentz force between two currents counterbalances the gravity acting on the plasma of the filament. The model was extended by van Tend & Kuperus (1978) with the introduction of a background coronal magnetic field so that the repulsive Lorentz force is counterbalanced by another Lorentz force produced by the external magnetic field. While exploring the equilibrium positions of coronal currents in active regions, it was shown that the straight current channel turns unstable against a small upward displacement when the repulsive force decreases more slowly with height than the confining force. Hereafter, this process will be referred to as the instability of the straight current channel. In the study by Kliem & Török (2006), the authors investigated conditions leading to torus instability, as they termed the similar process of expansion instability of the ring current channel, located inside an ambient magnetic field and partially submerged under the photosphere surface. The two instabilities represent the same process in different geometries of the current (straight versus toroidal) and are also equal to the well-known loss of equilibrium studied by, e.g., Forbes & Isenberg (1991; see Démoulin & Aulanier 2010; Kliem et al. 2014). A common property is that the current instability will occur when the external magnetic field B_{ex} sufficiently rapidly decreases with height h above the photosphere surface. A parameter that represents the rate of the magnetic field decrease is called the magnetic decay index, $n = -d\ln(B_{ex})/d\ln(h)$. It is assumed that this parameter may also play a key role in controlling the kinematics of eruptions (Török & Kliem 2007; Xu et al. 2012). In the approximation of an infinitely thin current channel, critical decay index values for the instability of the straight current and torus instability are equal to 1 and 1.5, respectively. Kliem & Török (2006) showed that at the limit of the self-similarly expanding current ring channel with a large aspect ratio (the ring's major radius to the current channel's radius), the critical decay index threshold for torus instability decreases slightly; in addition, taking into account the condition that the magnetic flux of the external magnetic field remains constant upon expansion of the ring leads to an increase of the threshold to $n = 2$. Démoulin & Aulanier (2010) generalized the consideration of both geometries and showed that for current channels expanding non-self-similarly with an arbitrary aspect ratio, the critical decay index values for the straight and ring current configurations become

[3] Corresponding author.

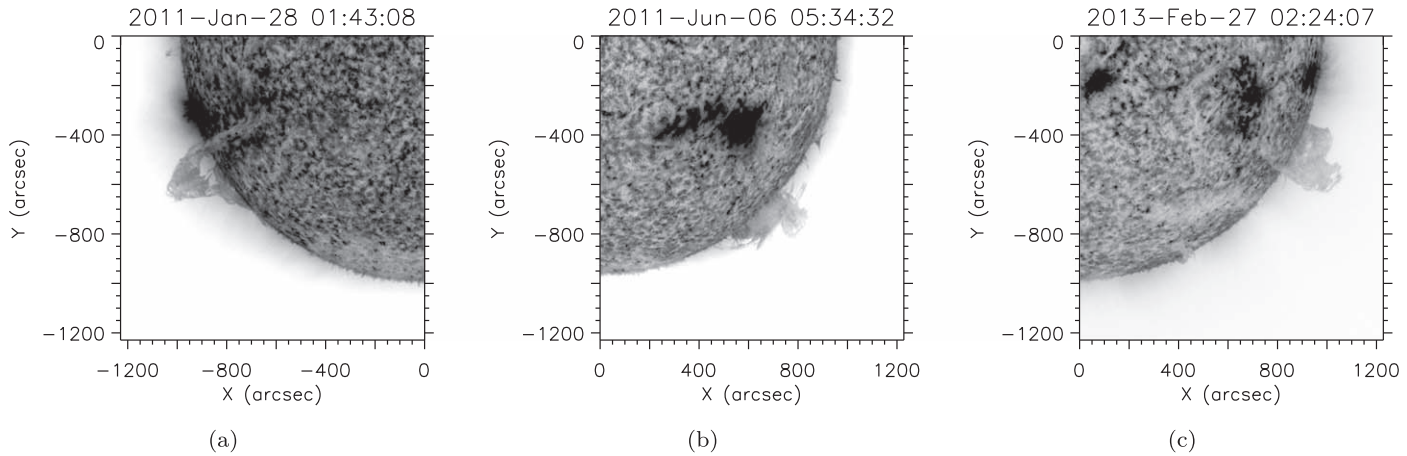

Figure 1. *SDO*/AIA 304 Å images of the studied EPs. (a) EP I, (b) EP II, (c) EP III. The time (UT), specified in the titles, corresponds to the estimated time of the eruption onset.

closer to each other and lie in the range [1.1, 1.3]. However, the authors noted that their results were obtained without the requirement of anchoring the ring current channel on the photosphere level. Imposing this condition, together with taking into account the influence of other current layers appearing in MHD simulations, may raise the threshold for torus instability. That was demonstrated in numerical experiments (Fan & Gibson 2007; Fan 2010) in which the estimated torus instability threshold was close to $n = 2$.

Various papers pay attention to the speed of the prominences or fine structure oscillations considering their physical nature (Dermendjiev et al. 1999; Okten et al. 2000; Petrov et al. 2004, 2007). The EPs are characterized by faster plasma motions and quasi-periodic velocity oscillations that remain unresolved (Duchlev et al. 2010a, 2010b). Previous studies that explored the relationship between the coronal magnetic decay index and solar eruptive events showed that the stable state of prominence is possible only below a certain height at which the instability of a straight current channel may develop (Filippov & Den 2001; Filippov & Zagnetko 2008; Shen et al. 2012; Xu et al. 2012; Filippov 2013; Filippov et al. 2014). In the study by McCauley et al. (2015), the authors considered more than 100 above-the-limb prominence eruptions. According to their findings, the major part of the eruptive events might be explained by the mechanism of the instability of a straight current, but the overall range of the obtained critical decay index values was rather wide, and some of the eruptive events should have developed due to the torus instability. In the study by Cheng et al. (2013), two filament eruptions originating in the active region were investigated, and it was shown that both events were triggered by the torus instability mechanism.

In our study, we consider three EPs. We compare the kinematic properties of the EPs and the spatial distribution of the magnetic decay index. For our analysis, we use the observational data provided by the Atmospheric Imaging Assembly (AIA; Lemen et al. 2012) and Heliospheric and Magnetic Imager (HMI; Schou et al. 2012) instruments on board the *Solar Dynamics Observatory* (*SDO*) spacecraft (Pesnell et al. 2012), as well as the Sun Earth Connection Coronal and Heliospheric Investigation (SECCHI; Howard et al. 2008) on the *Solar Terrestrial Relations Observatory* (*STEREO*) spacecraft (Kaiser et al. 2008). We reconstruct the coronal magnetic field in a potential-field approximation, which is a useful instrument for revealing the large-scale solar magnetic configuration (Altschuler & Newkirk 1969; Rudenko 2001; Riley et al. 2006; Platten et al. 2014; Wiegelmann et al. 2017).

2. Observations and Analysis

2.1. Kinematics of the Eruptions

For the analysis, we have selected three EPs matching the following criteria: (1) the prominences were situated outside active regions, (2) the eruptions occurred while the prominences were observed above the solar limb, and (3) the eruptions were associated with coronal mass ejections (CMEs). Figure 1 represents images of the selected EPs in the 304 Å channel by *SDO*/AIA. The images with an average cadence of 5 minutes are used to obtain height–time profiles of the eruptions that are represented in Figure 2 (top row), which shows the height of the corresponding EP's apex while the EP stayed in the *SDO*/AIA field of view, as well as the duration of the measurements: EP I, 322 ± 3 Mm (3.7 hr); EP II, 359 ± 2 Mm (4.42 hr); and EP III, 274 ± 1 Mm (4.15 hr). Measurement start times are specified in Table 1.

Usually, prominence eruptions consist of the initial activation phase with $v_{act} \approx 1$–$10\ km\ s^{-1}$ (Sterling & Moore 2004) and the eruptive phase with fast acceleration or gradually rising velocity (Neupert et al. 2001; Zhang et al. 2001; Zhang & Dere 2006), though the activation phase is not always required. The beginning of the eruptive phase is accepted to be the moment of sudden acceleration when the prominence reaches a certain critical height. Observational signatures for the start of the activation are changes in the brightness and twist of the prominence body near its feet (Vrsnak et al. 1991). The rising velocity increases up to a few hundred $km\ s^{-1}$. Basic information about the selected EPs is provided in Table 1. Often, the prominence has appeared hours or even days earlier, but we are not interested in its behavior before the beginning of the activation phase. The association between CMEs and their linear speeds is identified according to the *Solar and Heliospheric Observatory* (*SOHO*) Large Angle and Spectrometric Coronagraph Experiment (LASCO) CME Catalog.[4]

The information listed in the "Location" and "Class" columns of Table 1 is determined observationally. Prominences are divided by the latitude they appeared on into two groups—midlatitude prominences (MLPs) and polar crown prominences

[4] https://cdaw.gsfc.nasa.gov/CME_list/index.html

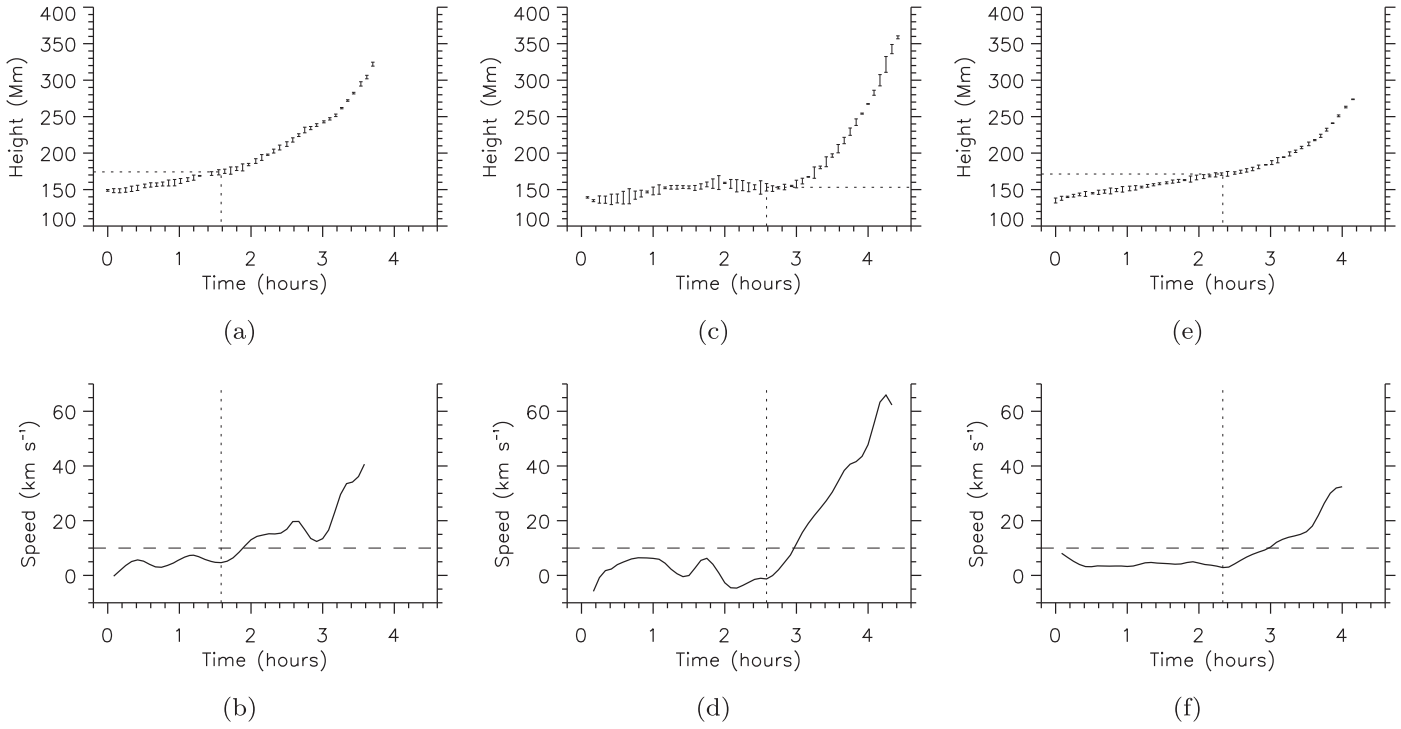

Figure 2. Height–time (top row) and corresponding speed–time (bottom row) profiles of the EPs. (a) and (b) EP I. (c) and (d) EP II. (e) and (f) EP III. For each particular case, the zero-point on the timeline corresponds to the starting moment of the height measurements, which are specified in Table 1. Vertical dotted lines mark the onset of the eruption process. Horizontal dashed lines designate the speed threshold, equal to 10 km s^{-1}.

Table 1
Details of the Explored EPs and Associated CMEs

No.	Date yyyy/mm/dd	T_{start} (UT)	CMEs		Location	Class	Mag. Date yyyy/mm/dd	Computational Domain length × width × height (Mm)
			Onset (UT)	v (km s^{-1})				
I	2011 Jan 28	00:00	05:00	170	MLP	QP	2011 Feb 1	590 × 440 × 300
II	2011 Jun 6	03:00	07:30	582	PCP	PP	2011 May 30	670 × 670 × 300
III	2013 Feb 27	00:00	04:00	622	MLP	QP	2013 Feb 25	730 × 540 × 300

Note. Abbreviations and designations: T_{start}, starting moment of height measurements; CMEs, coronal mass ejections; v, Onset: first appearance in *SOHO*/LASCO field of view; v: linear speed; MLP, midlatitude prominences; PCP, polar crown prominences; QP, quiescent prominence; PP, polar prominence; mag. date, the measurement date of the *SDO*/HMI magnetogram used for coronal magnetic field reconstruction. For all mag. dates, the time selected is 00:00 UT.

(PCPs). Despite some authors using the term PCP for those observed on the boundaries of polar coronal holes, we adopted the criteria of McCauley et al. (2015), who defined the boundary between MLPs and PCPs to be 50° heliographic latitude. The determination of the class is linked with the type of magnetic inversion lines that lie below the prominences (Mackay et al. 2008). Prominences could be classified into five groups: quiescent (QP), active, intermediate, polar (PP), or trans-equatorial. Our selection includes one PP and two QPs. All three explored EPs were symmetric (McCauley et al. 2015): they had a typical archlike shape during the eruption. According to the amount of prominence material that was ejected from the Sun, in the case of EP III, the eruption was full (more than 90% of prominence mass escapes the Sun), while in other cases, the eruptions were partial (all or part of the magnetic skeleton of the prominence erupts, with less than 90% of its mass being ejected as a result of mass draining and/or settling; Gilbert et al. 2007).

To determine the approximate heights where the eruptions started, we calculated corresponding speed–time profiles (Figure 2, bottom row) as follows. First, height measurements, nonuniformly distributed on the timeline, were interpolated on a regular grid with a 5 minute cadence. For noise suppression at each node of the grid, the average height was calculated using the value at that node and its two adjacent ones. The prominence's ascending speed was evaluated by applying the three-point differential scheme to the obtained average height distribution. We consider the latest local minimum on the speed–time profile, after which the speed started to increase and exceeded 10 km s^{-1}, as the onset of the eruption process. The same moment on the height–time profile determines the critical height at which the prominence has lost its equilibrium: EP I, 174 Mm; EP II, 153 Mm; EP III, 171 Mm. These values are noticeably greater than the average critical height for QPs (82 ± 42 Mm) and somewhat greater than the one for PCPs (101 ± 38 Mm) obtained in the study by McCauley et al. (2015). The provided prominence is anchored to the photosphere surface, and the greater the prominence's height, the more pronounced its archlike shape.

In our study, we are also using *STEREO*/SECCHI 304 Å images to determine the photosphere regions above which EPs were located, which is necessary for the reconstruction of the

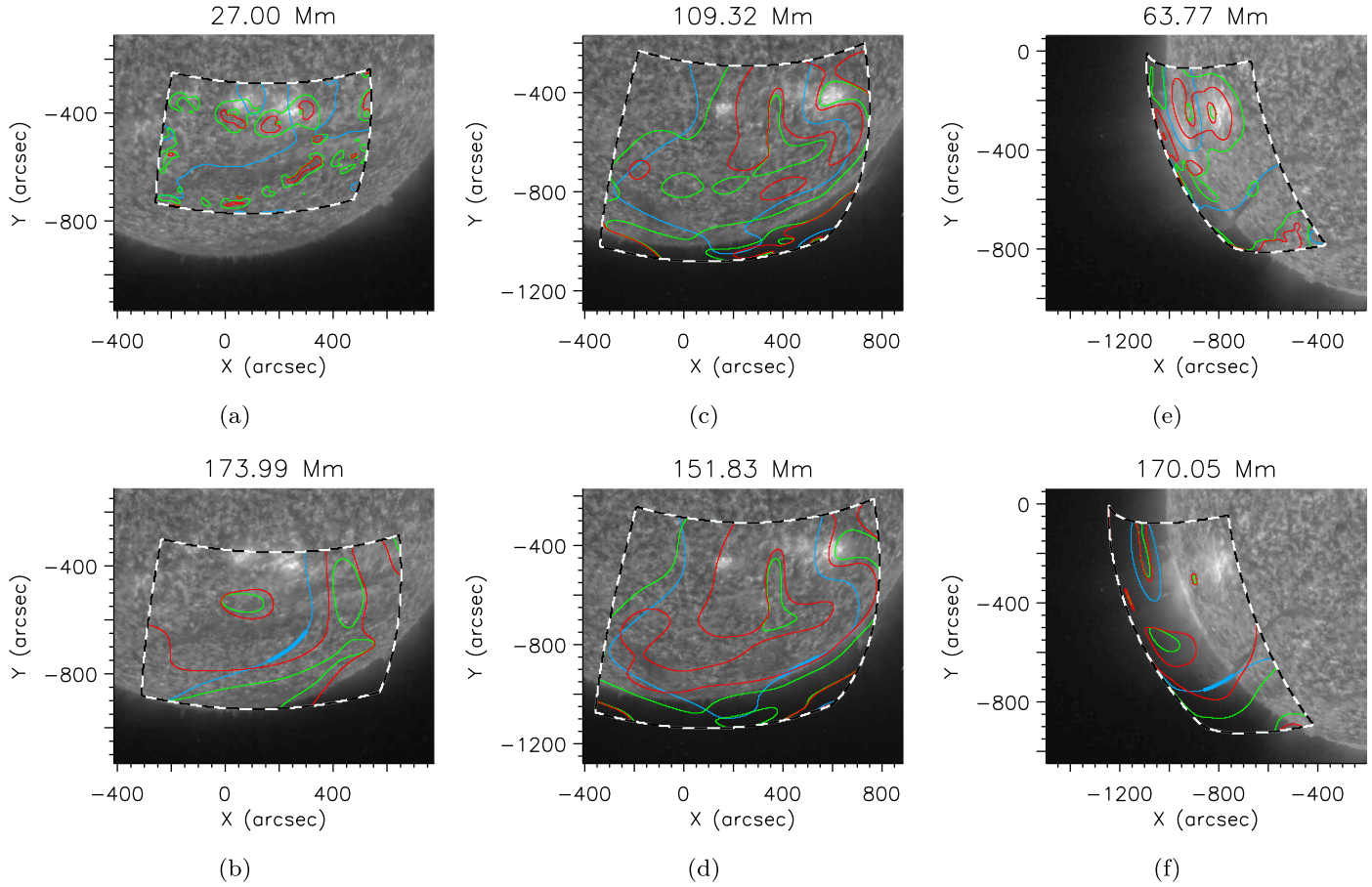

Figure 3. Distribution of the magnetic decay index and neutral line of the extrapolated magnetic field over the *STEREO*/SECCHI 304 Å images (shown as black-and-white background) at a given height over the photosphere. (a) and (b) EP I, *STEREO* B on 2011 January 28, 01:36 UT. (c) and (d) EP II, *STEREO* A on 2011 June 6, 05:26 UT. (e) and (f) EP III, *STEREO* A on 2013 February 27, 02:16 UT. The coordinate origin corresponds to the visible center of the solar disk. The thick black-and-white dashed contour is the boundary of the computational domain. Green and red contours mark the values of the magnetic decay index equal to 1 and 1.5, respectively. Blue contours represent the neutral line, and the thick segment approximately circumscribes the part of the neutral line that is closest to the prominence's apex.

coronal magnetic field and its subsequent validation. For all considered events, *STEREO* data provide images of the required quality, representing prominences with a highly distinguishable structure; see Figure 3. By considering the sequence of *STEREO* images corresponding to the eruption time in each case, we have identified EPs as they were observed from the *STEREO* spacecraft perspective. Figures 3(a) and (b) show EP I. It is elongated in an east–west direction near the $Y = -600''$ line in the plane of the sky and crosses the central meridian. Figures 3(c) and (d) show EP II, located in the western hemisphere close to the south. Figures 3(e) and (f) show EP III, which is clearly distinguishable near the eastern limb.

2.2. Magnetic Field Reconstruction

The coronal magnetic field is calculated using a potential-field extrapolation. For this purpose, we designed an algorithm that works in a spherical geometry and utilizes the Green's function solution of the Neumann external boundary-value problem for a sphere (see, e.g., Bogolubov & Kravtsov 1998). We use photosphere vector magnetograms provided by *SDO*/HMI with resolved π-ambiguity from which the radial component is determined and used as input boundary conditions. In all cases considered, the spatial resolution of the computational grid is equal to 3 Mm. Input photosphere magnetograms are smoothed accordingly. This makes effective noise suppression without affecting the large-scale magnetic field and reduces computation time. The extrapolation method works with a predefined area of the photosphere; on the rest of the surface, the radial magnetic field is considered equal to zero.

We consider eruptions that occurred when the prominences were located above the solar limb. Because of this, it is impossible to use the magnetograms corresponding to the photosphere regions below the prominences for the time of the eruption onset due to the projection effect. We perform magnetic field extrapolation over the same regions using magnetograms measured several days before (west limb events) or after (east limb event) the eruptions. We assume that the large-scale magnetic field in the regions of quiescent prominence formation is slowly evolving and probably will not change its structure significantly after several days. Information about the magnetograms used and the size of the computational domains employed for magnetic field extrapolation is presented in the last two columns of Table 1.

2.3. Magnetic Decay Index

In the case where the mechanism of electric current instability inside the ambient magnetic field is responsible for the eruption, it is possible to predict the prominence's behavior,

depending on the steepness of the magnetic field decrease with height. This dependence can be reflected by a parameter called the magnetic decay index:

$$n = -\frac{h}{B_t}\frac{dB_t}{dh}. \quad (1)$$

Here, B_t is the transverse component of the ambient magnetic field, and h is the height above the photosphere. Further, we investigate the spatial distribution of the magnetic decay index, computed for the extrapolated potential magnetic field. In the study by van Tend & Kuperus (1978), the authors found that the electric current cannot be confined by the ambient magnetic field and loses its equilibrium in the regions where the magnetic decay index exceeds a certain critical value. Different current configurations have their specific critical thresholds. Following studies by van Tend & Kuperus (1978) and Kliem & Török (2006), at the limit of the infinitely thin current channel, one can specify two characteristic critical thresholds of the magnetic decay index: $n = 1$ for the instability of the straight current channel and $n = 1.5$ for the torus instability.

3. Discussion

Our aim is to investigate the spatial distributions of the computed magnetic decay index and compare these distributions with obtained height–time profiles. Information on the 3D structure of the extrapolated magnetic field allows one to calculate the magnetic decay index everywhere inside the computational domain. Prominences in a stable state are oriented along a neutral line of the ambient magnetic field. This is in agreement with the model by van Tend & Kuperus (1978), where the equilibrium of the electric current is stable against small transverse displacements due to the restoring Lorentz force. Thus, only the regions close to the neutral line are of specific interest. Moreover, a particular segment of the neutral line that is near the observed prominence's apex should be determined. For this purpose, it is necessary to take into account observational data close to the eruption time.

Above-the-limb observations provided by *SDO* are not suitable for solving a problem of this kind. Instead, we are using *STEREO*/SECCHI images. In each particular case, these images allowed us to define the Carrington coordinates of the sufficiently large photosphere region below the observed prominence and build the computational domain in the coronal space. Then, these predefined domains were rotated several days before or after the eruption to the time when they were not very far from the solar disk center in the *SDO* field of view in order to take the photosphere boundary conditions from the *SDO*/HMI data. Solar differential rotation was not taken into account.

Figure 3 shows the neutral line of the extrapolated magnetic field and characteristic contours representing the spatial distribution of the magnetic decay index overlaid on the *STEREO*/SECCHI images. Contours are plotted on the spherical layers at a specified height above the photosphere. In all cases, the neutral line coincides sufficiently well with the position of the prominence. Figures 3(e) and (f) represent a side view of the EP III. From this perspective, it can be seen that the prominence has an archlike configuration. Different parts of the prominence are located at different heights and are better traced by the neutral line plotted on the layers with a corresponding height. These comparisons justify applying the potential-field extrapolation for obtaining the spatial distribution of the coronal magnetic field ambient to the EPs. Also, it allows one to make a conclusion that the prominences ascended along the neutral surfaces up to the height where instability has developed.

The segment of the neutral line that is presumably the nearest to the prominence's apex is determined following a simple criterion. First, the highest layer where the neutral line still overlays the prominence is selected (see Figure 3, bottom row). Then, a straight line passing through the solar center and a point of coincidence of the neutral line on the selected layer with the prominence is drawn. Finally, on any other layer, a point on the neutral line closest to this straight line is determined. This point is considered the center of the neutral line segment with a length approximately equal to 200 Mm.

Figure 4 represents the spatial distribution of the magnetic decay index. To avoid the projection effect, the coordinate origin is placed at the center of the bottom boundary of the computational domain. Minimal and maximal values of the magnetic decay index are limited to 0 and 5, respectively. According to our calculations, starting from heights where small-scale magnetic structures disappear, in all cases, the magnetic decay index is gradually increasing with height in the area around the predefined segment of the neutral line. Figure 5 shows the distribution of the minimum, maximum, and average value of the decay index along the segment length for the 80–180 Mm height range. At heights of about 80 Mm, the value of the magnetic decay index becomes greater than unity throughout the entire length of the segment. For each particular case, the obtained height difference with the prominence's apex by the time of the eruption onset is somewhat greater than the prominence's vertical cross section, estimated from *SDO*/AIA images and approximately equal to 80 Mm, that is typical for a quiescent prominence in the last stage of its evolution (Rompolt 1990). Thus, the mechanism of the instability of a straight electric current seems to not be applicable for the explanation of the considered eruptive events.

At heights of 120–160 Mm, the neutral line segments reach regions of space where the magnetic decay index exceeds another critical threshold equal to 1.5, which is specific for the torus instability. For EP II and EP III, the central region of the segment trespasses the threshold first, and, at a relatively short height range, a considerable part of the segment enters the zone with $n > 1.5$. In the case of EP I, this process starts on the northwest side of the segment and is going more smoothly. This is reflected in Figure 5, where in the case of EP I, the decay index has a relatively wide distribution over the segment for all presented height ranges; in the case of EP II, the maximum and average values are close; and in the case of EP III, the decay index distribution is very narrow. It is interesting to note that EP I was followed by a slow-speed CME, while EP II and EP III were associated with average-speed CMEs (see Table 1). For EP II, the height at which the averaged decay index becomes greater than 1.5 is only slightly less than the estimated height of the prominence's apex by the time of the eruption onset. For the rest of the cases, this critical height is noticeably below the apex, but the corresponding height difference is only about half of the prominence's vertical cross section. This makes possible the following interpretation of the considered eruptive events. The electric current inside the prominence slowly ascended along the neutral line of the ambient coronal magnetic field until it lost its equilibrium,

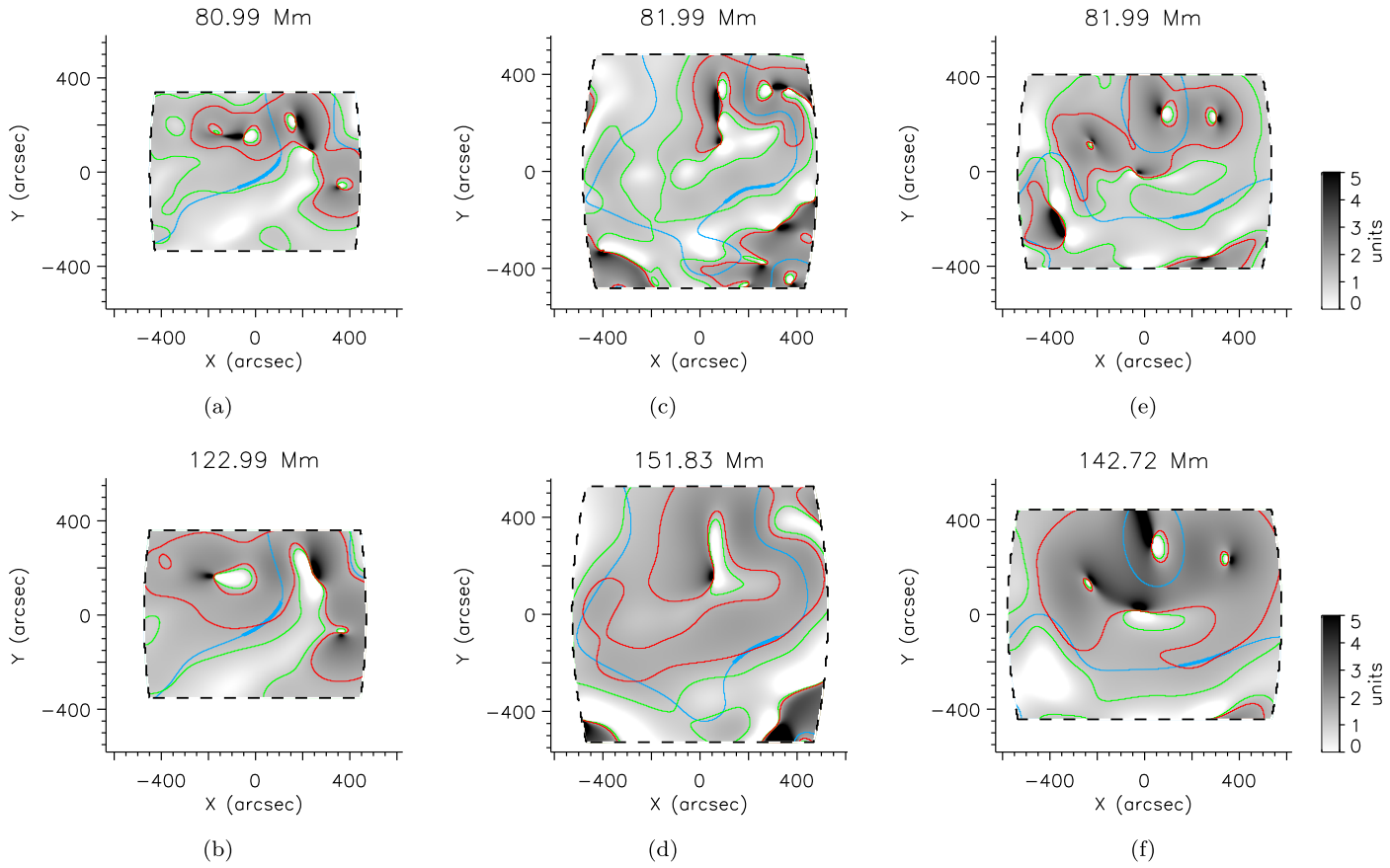

Figure 4. Top view of the distribution of the magnetic decay index and neutral line of the extrapolated magnetic field at a given height over the photosphere. The magnetic decay index is shown as the black-and-white background, and the maximal and minimal values are limited to 0 and 5, respectively. (a) and (b) EP I. (c) and (d) EP II. (e) and (f) EP III. The coordinate origin corresponds to the center of the bottom boundary of the computational domain. Color-coded contours are the same as in Figure 3. The bottom row shows the distribution of the magnetic decay index at the height where the decay index, averaged over the thick segment of the neutral line, first exceeded the critical threshold equal to 1.5.

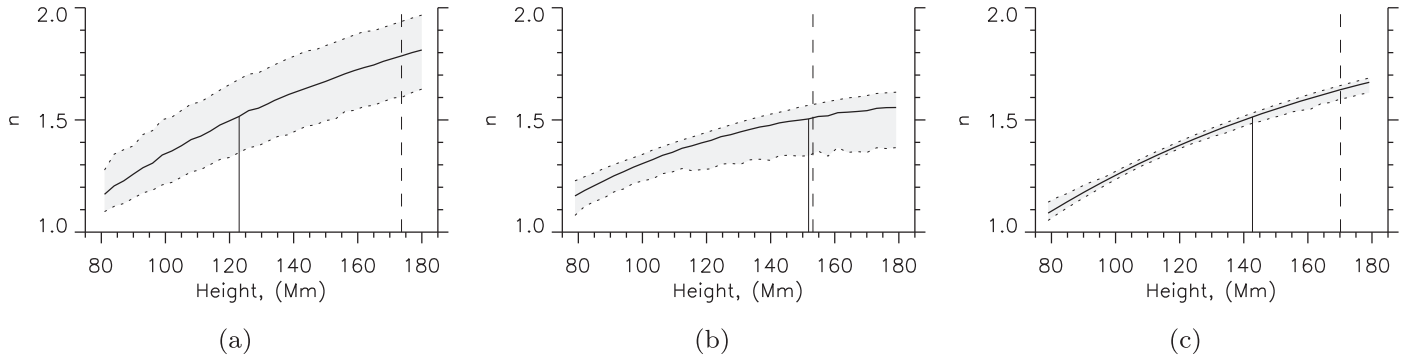

Figure 5. Height distribution of the magnetic decay index over the predefined segment of the neutral line. (a) EP I. (b) EP II. (c) EP III. The upper and lower dotted lines correspond to the maximum and minimum values, respectively. The thick solid line shows the value averaged over the segment's length. The solid vertical line marks the height at which the averaged decay index first exceeded the critical threshold equal to 1.5. The dashed vertical line marks the estimated height of the prominence's apex by the time of the eruption onset.

reaching the height where the magnetic decay index exceeded the critical value equal to 1.5. Taking into account that all considered prominences had an archlike shape by the time of the eruption onset, we assume that the torus instability mechanism was responsible for the eruptions.

4. Conclusions

We considered three cases of solar prominence eruptions. Eruptions occurred when the prominences were located above the solar limb. In each case, this allowed us to build height–time and speed–time profiles of the prominence's apex and determine the approximate height at which the eruption started. We reconstructed a coronal magnetic field, ambient to the prominences, in a potential-field approximation and obtained the spatial distribution of the magnetic decay index. For all considered cases, we have found that the height where the magnetic decay index has exceeded the critical threshold equal to 1.5 is either close to or somewhat lower than the estimated height of the prominence's apex by the time of the eruption onset. This is consistent with the assumption that the electric current was located inside the

prominence. Considering that all prominences had an archlike shape, this indicates the torus instability as a possible mechanism of the considered eruptive events.

The authors are grateful to the science teams of the *SDO* and *STEREO* projects for the observational data and to the anonymous referee, whose valuable comments helped to improve the text.

This study is partially supported by the following projects: "The origin of solar energetic particles: solar flares versus coronal mass ejections," cofunded by the Russian Foundation for Basic Research with projects No. 17-52-18050 and the National Science Fund of Bulgaria under contract No. DNTS/Russia 01/6 (2017 June 23) (I.M., Ts.Ts.), 18-32-20165 mol_a_ved (I.M.); the program of Basic Research No. II.16 (I.M.); the program of Basic Research of the RAS Presidium KP19-270 (I.M.); and "Research on active solar processes during and beside total solar eclipses," funded by the National Science Fund of Bulgaria under contract No. KP-06-H28/4 (2018 December 8) (Ts.Ts.).

ORCID iDs

Ivan Myshyakov https://orcid.org/0000-0002-8530-7030
Tsvetan Tsvetkov https://orcid.org/0000-0002-5838-5244

References

Altschuler, M. D., & Newkirk, G. 1969, SoPh, 9, 131
Babcock, H. W., & Babcock, H. D. 1955, ApJ, 121, 349
Bogolubov, A. N., & Kravtsov, V. V. 1998, in Tasks on Mathematical Physics, ed. A. G. Sveshnikov et al. (Moscow: Moscow Univ. Press)
Cheng, X., Zhang, J., Ding, M. D., et al. 2013, ApJL, 769, L25
Démoulin, P., & Aulanier, G. 2010, ApJ, 718, 1388
Dermendjiev, V. N., Detchev, M., Petrov, N., & Rompolt, B. 1999, in Structure, internal motion and oscillation of a quiescent prominence, JOSO Annu. Rep. 1998, 122
Duchlev, P., Koleva, K., Dechev, M., et al. 2010a, BlgAJ, 14, 89
Duchlev, P., Koleva, K., Kokotanekova, J., et al. 2010b, BlgAJ, 13, 47
Fan, Y. 2010, ApJ, 719, 728
Fan, Y., & Gibson, S. E. 2007, ApJ, 668, 1232
Filippov, B. 2013, ApJ, 773, 10
Filippov, B., & Zagnetko, A. 2008, JASTP, 70, 614
Filippov, B. P., & Den, O. G. 2001, JGR, 106, 25177
Filippov, B. P., Martsenyuk, O. V., Den, O. E., & Platov, Y. V. 2014, ARep, 58, 928
Forbes, T. G., & Isenberg, P. A. 1991, ApJ, 373, 294
Gilbert, H., Kilper, G., & Alexander, D. 2007, ApJ, 671, 978
Howard, R. A., Moses, J. D., Vourlidas, A., et al. 2008, SSRv, 136, 67
Kaiser, M. L., Kucera, T. A., Davila, J. M., et al. 2008, SSRv, 136, 5
Kilper, G., Gilbert, H., & Alexander, D. 2009, ApJ, 704, 522
Kliem, B., Lin, J., Forbes, T. G., Priest, E. R., & Török, T. 2014, ApJ, 789, 46
Kliem, B., & Török, T. 2006, PhRvL, 96, 255002
Kuperus, M., & Raadu, M. A. 1974, A&A, 31, 189
Lemen, J. R., Title, A. M., Akin, D. J., et al. 2012, SoPh, 275, 17
Mackay, D. H., Gaizauskas, V., & Yeates, A. R. 2008, SoPh, 248, 51
McCauley, P. I., Su, Y. N., Schanche, N., et al. 2015, SoPh, 290, 1703
Neupert, W. M., Thompson, B. J., Gurman, J. B., & Plunkett, S. P. 2001, JGR, 106, 25215
Okten, A., Dermendjiev, V. N., Petrov, N. I., Ozisik, T., & Esenoglu, H. H. 2000, BlJPh, 27, 85
Pesnell, W. D., Thompson, B. J., & Chamberlin, P. C. 2012, SoPh, 275, 3
Petrov, N., Duchlev, P., Rompolt, B., & Rudawy, P. 2004, in IAU Symp. 223, Multi-Wavelength Investigations of Solar Activity, ed. A. V. Stepanov, E. E. Benevolenskaya, & A. G. Kosovichev (Cambridge: Cambridge Univ. Press), 293
Petrov, N., Duchlev, P., Rompolt, B., & Rudawy, P. 2007, BlgAJ, 9, 93
Platten, S. J., Parnell, C. E., Haynes, A. L., Priest, E. R., & Mackay, D. H. 2014, A&A, 565, A44
Riley, P., Linker, J. A., Mikić, Z., et al. 2006, ApJ, 653, 1510
Rompolt, B. 1984, AdSpR, 4, 357
Rompolt, B. 1990, HvaOB, 14, 37
Rudenko, G. V. 2001, SoPh, 198, 5
Schou, J., Scherrer, P. H., Bush, R. I., et al. 2012, SoPh, 275, 229
Shen, Y., Liu, Y., & Su, J. 2012, ApJ, 750, 12
Sterling, A. C., & Moore, R. L. 2004, ApJ, 602, 1024
Török, T., & Kliem, B. 2007, AN, 328, 743
van Tend, W., & Kuperus, M. 1978, SoPh, 59, 115
Vrsnak, B., Ruzdjak, V., & Rompolt, B. 1991, SoPh, 136, 151
Wiegelmann, T., Petrie, G. J. D., & Riley, P. 2017, SSRv, 210, 249
Xu, Y., Liu, C., Jing, J., & Wang, H. 2012, ApJ, 761, 52
Zhang, J., & Dere, K. P. 2006, ApJ, 649, 1100
Zhang, J., Dere, K. P., Howard, R. A., Kundu, M. R., & White, S. M. 2001, ApJ, 559, 452